Article

Phase Separation in the Double Perovskite Sr$_2$FeNbO$_{6-\delta}$

Daniil Popov [1], Ruslan Batulin [2], Mikhail Cherosov [2], Farit Vagizov [2], Almaz Zinnatullin [2], Tatiana Chupakhina [3], Yuliya Deeva [3], Tanmoy Maiti [4] and Rushana Eremina [1,*]

[1] Zavoisky Physical-Technical Institute, Federal Research Center "Kazan Scientific Center of RAS", 420029 Kazan, Russia; kazan-city.dvpopoff@yandex.ru

[2] Institute of Physics, Kazan (Volga Region) Federal University, 420008 Kazan, Russia; tokamak@yandex.ru (R.B.); mcherosov@gmail.com (M.C.); vagizovf@gmail.com (F.V.); almaz.zinnatullin@gmail.com (A.Z.)

[3] Institute of Solid State Chemistry of the Russian Academy of Sciences (UB), 620990 Yekaterinburg, Russia; chupakhina@yandex.ru (T.C.); juliahik@mail.ru (Y.D.)

[4] Department of Materials Science and Engineering, Indian Institute of Technology, Kanpur 208016, India; tmaiti@iitk.ac.in

* Correspondence: reremina@yandex.ru; Tel.: +07-(843)-272-05-03

Abstract: The ceramic perovskite Sr$_2$FeNbO$_{6-\delta}$ was synthesized via the solution combustion precursor method. X-ray phase analysis showed that the sample is single-phase and does not contain impurities. The specific heat capacity and the Mössbauer spectra were measured for the Sr$_2$FeNbO$_{6-\delta}$ ceramic in the temperature range of 4–300 K. The observation of an asymmetric doublet in the Mössbauer spectra and the literature data on the magnetic susceptibility indicated the presence of two magnetic subsystems in Sr$_2$FeNbO$_{6-\delta}$ with antiferromagnetic exchange interactions. Based on the analysis of the temperature dependence of the specific heat capacity, we determined the Debye and Einstein temperatures.

Keywords: Mössbauer spectra; specific heat capacity; double perovskite

1. Introduction

RE$_2$Me1Me2O$_6$ double-perovskite oxides, where *Me1* and *Me2* are different 3D transition metals, are finding more and more applications. Over the past year, several excellent reviews on the study of various properties of double perovskites have been published. Recent advances in the characterization of the crystal structure, magnetic properties, and cryogenic magnetocaloric effect are summarized in [1]. The halide double perovskite with structural flexibility, as well as lower toxicity and higher stability, attracted the attention of the scientific community and stimulated the research on halide double perovskites with a lead-free A$_2$B(I)B(III)X$_6$ composition [2]. The problems arising in the design and synthesis of double perovskites and possible ways to overcome them are discussed in [3]. Promising applications of double perovskites for the development of high-performance photodetectors are considered in [4].

The double perovskite Sr$_2$FeNbO$_6$ compound is being actively studied in connection with its possible application for boosting the charge separation for efficient photocatalytic CO$_2$ reduction in the heterostructure of Cs$_2$AgBiBr$_6$/Sr$_2$FeNbO$_6$ [5]. Electrochemical impedance spectroscopy measurements indicated that ZrO$_2$-stabilized Sr$_2$FeNbO$_6$-Y$_2$O$_3$ can be used as a hydrogen electrode in high-temperature steam electrolysis [6]. Fe^{3+} atoms in the cubic lattice of Sr$_2$FeNbO$_6$ play a crucial role in yielding high visible-light photocatalytic activity [7]. For photocatalytic applications such as pure hydrogen production and solar-to-electrical energy conversion, compounds with an energy band gap (E$_g$) between 1.4 and 2 eV are needed. The Sr$_2$FeNbO$_6$ ceramic with an E$_g$ of 1.9 eV has great potential in these applications [8]. The possibility of its use in industrial applications was considered in [9] as an alternative fuel electrode in solid oxide electrolysis cells due to their high

chemical stability. The review [10] summarizes recent studies on $Sr_2Me1Me2O_6$-based double perovskites for high-temperature thermoelectric power generation. It was shown that the decoupling of phonon-glass and electron-crystal behaviors in oxides is possible by reducing thermal conductivity due to the induced dipolar glassy state as a result of relaxor ferroelectricity [10]. It should be noted that the ionic radii of iron and niobium in a sixfold environment almost coincide (0.67 Å and 0.66 Å, respectively), which is also realized for compounds with Mo and Fe [11]. Therefore, the authors of [11] suggest using thin films to obtain an ordered distribution of elements. The B-site ordering double perovskites has also been widely reported in room-temperature electrolysis, such as water splitting [12]. Doping phosphorus into perovskites is an effective way to develop high-performance electrocatalysts for the oxygen reduction reaction [13].

Double perovskites of Sr_2FeNbO_6 were studied in multiple works [14–16]. However, these papers show different results of structural and magnetic studies. According to [17], $Sr_2FeNbO_{6-\delta}$ prepared using a conventional solid-state method features the orthorhombic structure *Pnma* (a = 5.62 Å, b = 7.96 Å, and c = 5.61 Å). The tetragonal structure with space group I4/m (a = 5.61 Å and c = 7.97 Å) was obtained via the conventional ceramic method [18]. The orthorhombic structure with space group *Pnma* and lattice parameters a = 5.6082(9) Å, b = 7.9642(1) Å, and c = 5.6084(9) Å was reported in [14]. The cubic structure with a = 3.99 Å was found in [19]. Sr_2FeNbO_6 has an orthorhombic unit cell with a *Pbnm* space group, and their lattice constants are a = 0.56077(9) nm, b= 0.56038(9) nm, and c = 0.78991(8) nm from neutron diffraction data [16]. The crystal structure is presented in the paper [8]. Different transition temperatures have been reported: in [15], $Sr_2FeNbO_{6-\delta}$ was shown to experience a spin glass transition at T_G = 32.5 K; in [16], a spin glass transition was observed at T_G = 20 K. The established phase transition temperatures for a double perovskite Sr_2FeNbO_6 differ strongly from the ordering temperatures of its constituent single perovskite. $SrFeO_3$ has a cubic structure with a = 3.85 Å and an antiferromagnetic transition at T_N = 134 K [20]. Bulk $SrNbO_3$ is not stable under ambient conditions [21].

Mössbauer spectra of Sr_2FeNbO_6 were measured at 298 K and 6 K in [14]. The authors concluded that the symmetry at the Fe site in the lattice is no longer cubic. The experimental spectra were reproduced via the single-doublet fitting at room temperature with δ = 0.390(1) mm/s, ε = 0.250(1) mm/s, Γ = 0.462(4) mm/s and δ = 0.481(10) mm/s, ε = 0.001(9) mm/s, Γ = 0.894(37) mm/s, and B_{hf} (T) = 48.71(7) at 6 K. However, the temperature dynamics and fluctuations of the spin moment have not been studied. The purpose of the present research is to study magnetic and transport properties of the $Sr_2FeNbO_{6-\delta}$ ceramics in the temperature range of 4–300 K via the Mössbauer method and the specific heat data analysis.

2. Materials and Methods

Double perovskite Sr_2FeNbO_6 was obtained via pyrolysis of nitrate-organic mixtures of the following components: $Sr(NO_3)_2$ (strontium nitrate, chemically pure grade), Fe (carbonyl, ultra-pure grade), Nb_2O_5 (niobium oxide, chemically pure grade), NH_4OH (chemically pure grade), HNO_3 (chemically pure grade), and $C_5H_7(OH)_5$ (chemically pure grade). The compound $C_5H_7(OH)_5$ (pentanpentaol, xylitol) as an organic component promotes the dissolution of niobium oxide in an alkaline medium and simultaneously ensures the pyrolysis process in the self-ignition mode of the solution.

Iron nitrate (II) is obtained by dissolving a stoichiometric amount of carbonyl iron in dilute (1:1) nitric acid with low heating. $Sr(NO_3)_2$ was dissolved in distilled water. The resulting solutions were mixed. Next, a stoichiometric amount of niobium oxide was added to the reaction mixture. With constant stirring, the solution was neutralized to pH = 7 with ammonia, then the pH of the solution was slowly adjusted to 12.5. After that, with constant stirring, the compound $C_5H_7(OH)_5$ was added to the mixture in the ratio Nb_2O_5:$C_5H_7(OH)_5$ = 1:5 mol. The reaction mass was kept for 9–10 h until maturation. The next day, another 4–5 g of $C_5H_7(OH)_5$ was added as an organic fuel, and the solution was evaporated before the combustion process started. The pyrolysis product is a black

ultrafine powder, which was calcined at 950 °C for 1.5–2 h to remove carbon impurities. The resulting sample was pelletized and calcined at 1100–1150 °C for 8 hours. The total synthesis time was two days.

X-ray examination (Figure 1) was performed using a Shimadzu XRD-7000 S automatic diffractometer with an exposure time of 3–5 s per point. X-ray pattern processing was performed with the FULLPROF-2018 software. According to X-ray diffraction data, the resulting product is the double perovskite $Sr_2FeNbO_{6-\delta}$. We have not detected any foreign impurities and impurities of unreachable substances. The $Sr_2FeNbO_{6-\delta}$ phase diffraction pattern can be described based on two space groups. The first of which is the Pm3m space group with a = 3.96748(8)Å, which is consistent with [19]. X-ray diffraction pattern is presented for the cubic group in Figure 1a. The Rietveld refined crystal structural parameters are summarized in Table 1. The second possible description of the X-ray diffraction pattern is given within the Pbnm space group and lattice parameters $a = b$ = 5.605(7); c = 7.929(4) V and Å^3 = 250.28(2). An X-ray diffraction pattern is presented for the Pbnm group in Figure 1b. The Rietveld refined crystal structural parameters are summarized in Table 2.
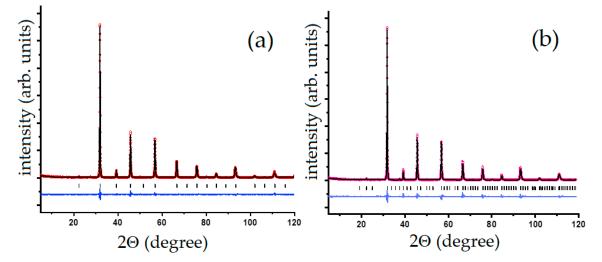

Figure 1. X−ray diffraction pattern of $Sr_2FeNbO_{6-\delta}$ in (**a**) Pm3m space group and (**b**) Pbnm space group. The blue line is a plot of the difference between calculated and observed X−ray pattern.

Table 1. The Rietveld refinement for $Sr_2FeNbO_{6-\delta}$ in Pm3m space group.

Atom	Site	x	y	z	B_{iso} (Å^2)	Occupancy
Sr	1b	0.5	0.5	0.5	1.29(9)	1
Fe	1a	0	0	0	0.44(3)	0.5
Nb	1a	0	0	0	0.44(3)	0.5
O1	3d	0.5	0	0	2.35(8)	3.01(4)

Selected bond lengths (Å)
Nb/Fe-O   1.983(1) × 6
Sr-O   2.805(1) × 12
R-factors: R_{wp} = 7.85%, R_{exp} = 8.74%, R_B = 2.58, R_f = 2.99, and χ^2 = 1.85.

Table 2. The Rietveld refinement for $Sr_2FeNbO_{6-\delta}$ in Pbnm space group.

Atom	Site	x	y	z	Occupancy
Sr	4c	−0.003(5)	−0.502(1)	0.25	1
Fe	4a	0.5	0	0	0.5
Nb	4a	0.5	0	0	0.5

Table 2. *Cont.*

Atom	Site	x	y	z	Occupancy
O1	4c	0.005(1)	0.564(4)	0.25	0.6795(4)
O2	8d	0.254(1)	0.247(2)	0.496(4)	1.007(3)

Selected bond lengths (Å)
Fe/Nb-O1   1.992(3)
Fe/Nb-O2a   1.975(1)
Fe/Nb-O2b   1.998(6)
Sr-O1   2.631(1)
Sr-O2a   2.779(3)
Sr-O2b   2.846(5)
Sr-O2c   2.807(3)
R-factors: R_{wp} = 15.3%, R_{exp} = 8.54%, R_B = 5.63, R_f = 5.10, and χ^2 = 2.56.

XFA measurements performed via the Bruker S2 Ranger X-ray fluorescence spectrometer allowed us to determine the elements ratio as Fe/Sr/Nb = 0.17:0.55:0.28. Based on the electrical neutrality of the sample, we calculated the oxygen content as 5.4 for the Fe^{3+}, Sr^{2+}, and Nb^{5+} valences. The real formula of the sample is $Sr_2NbFe_{0.6}O_{5.4}$. Oxygen deficiency is observed in the sample according to XFA measurements, so the Pbnm space group is more suitable for describing the structure $Sr_2NbFe_{0.6}O_{5.4}$.

Mössbauer studies of the $Sr_2FeNbO_{6-\delta}$ sample were performed on a WissEl spectrometer (Germany) operating in the constant acceleration regime. As a source of resonant gamma radiation, we used ^{57}Co in a rhodium matrix with an activity of ~ 50 mCi (Ritverc, St. Petersburg, Russia). For low-temperature Mössbauer measurements, a CFICEV flow cryostat (ICE Oxford, UK) with a CryoCon 32B temperature controller was used, which makes it possible to maintain the sample temperature with an accuracy of ± 0.2 K. The absorber was made from a finely ground powder of the investigated compound mixed with boron nitride to obtain a sample uniform in thickness and to disorder the orientation of microcrystallites. For measurements, we used a sample with a surface density of 27 mg/cm^2. The velocity scale of the spectrometer was calibrated using the spectrum of a thin metallic iron foil. The values of isomer shifts are given relative to the gravity center of the metallic iron spectrum at room temperature. The spectra were processed using the SpectrRelax 2.1 software [22].

Specific heat capacity measurements were performed using the PPMS-9 device in the 5–300 K temperature range at 0 and 9 T.

3. Results

3.1. Mössbauer Measurements

Mössbauer measurements were performed in a wide temperature range spanning from room temperature to the temperature of liquid nitrogen and liquid helium. The profile of the $Sr_2FeNbO_{6-\delta}$ spectrum at room temperature is an asymmetric doublet (Figure 2) with slightly higher line amplitude in the region of low velocities compared to the other doublet line.

It should be noted that the lines of the paramagnetic doublet are noticeably broadened. This broadening is most probably driven by the random distribution of Fe^{3+} and Nb^{5+} ions at the sites of the crystal lattice, which leads to the appearance of a significant electric field gradient (EFG) on the nuclei of Fe ions and their distribution in accordance with a combination of possible local environments of the resonant atom with niobium and iron ions. Therefore, to fit the experimental spectra, we used the assumption that there is a distribution of quadrupole splitting and isomeric shifts on the nuclei of resonant atoms. Figure 2a shows the Mössbauer spectrum of the $Sr_2FeNbO_{6-\delta}$ sample at room temperature along with its best fit, which takes into accounts the distribution of hyperfine parameters.
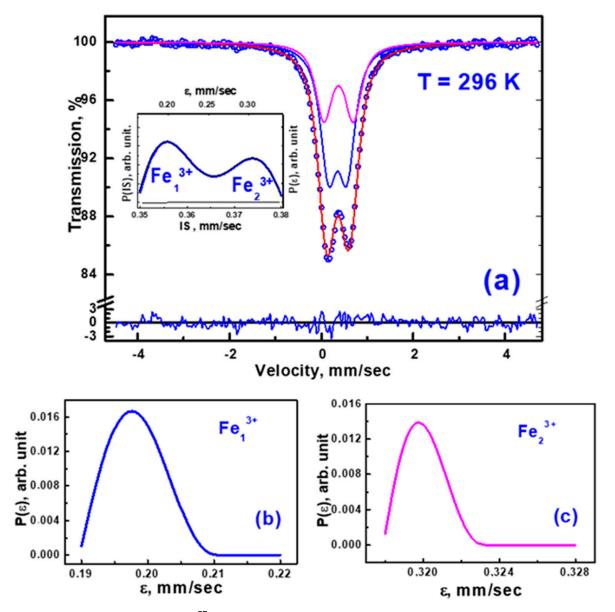
Figure 2. (**a**) ^{57}Fe Mössbauer spectrum of $Sr_2FeNbO_{6-\delta}$ measured at room temperature: experiment (blue dots) and its best fit (red line). The inset shows the reconstructed distribution functions of hyperfine parameters IS and $\varepsilon = QS/2$. The blue and magenta lines show the best fits of the partial components corresponding to the Fe_1^{3+} and Fe_2^3 centers. Also shown is the difference between the experimental spectrum and its best fit normalized to the statistical uncertainty in the range of $\pm 3\sigma$. (**b**,**c**) Reconstructed distribution functions of the quadrupole shift ε of Fe_1^{3+} (**b**) and Fe_2^3 (**c**) doublets.

Figure 3 shows the Mössbauer spectra of $Sr_2FeNbO_{6-\delta}$ in the temperature range from 296 K to 80 K. The red lines show the best fits of the spectra based on the two-doublet model with a distribution of quadrupole shifts. In Figure 3, the blue and magenta solid lines show the partial components corresponding to the Fe_1^{3+} and Fe_2^{3+} centers. Lowering the temperature to 50 K preserves the doublet structure of the spectra. At the same time, there is a weak temperature dependence of the average value of the quadrupole shift $<\varepsilon>$ and the content of Fe_1^{3+} and Fe_2^{3+} doublets (Figure 4).
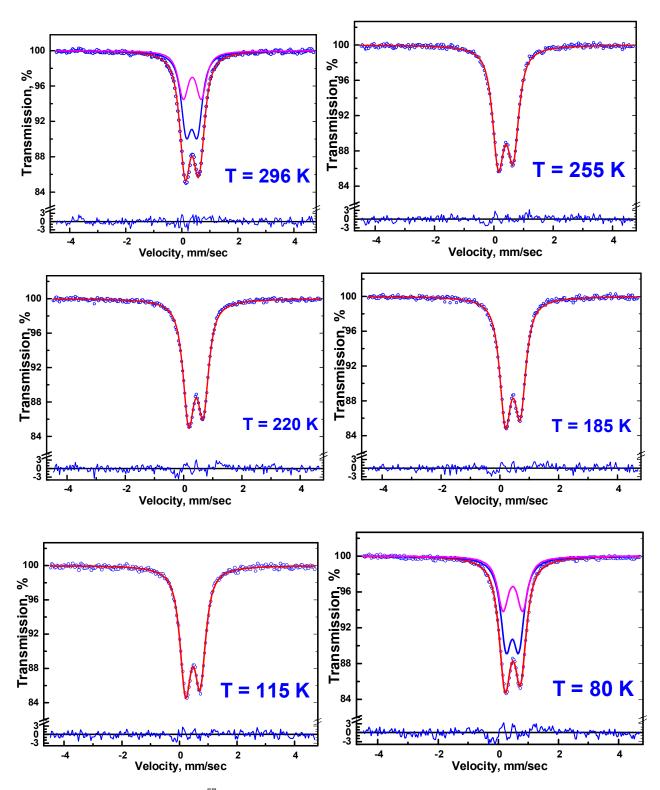
Figure 3. ^{57}Fe Mössbauer spectra of $Sr_2FeNbO_{6-\delta}$ measured at different temperatures: experiments (blue dots) and their best fits (red lines). The blue and magenta lines show the best fits of the partial components corresponding to the Fe_1^{3+} and Fe_2^3 centers. Also shown are the differences between the experimental spectra and their best fits normalized to the statistical uncertainty in the range of $\pm3\sigma$.
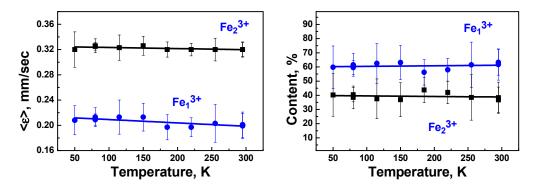
Figure 4. Temperature dependencies of the average quadrupole shift $<\varepsilon>$ (**left** panel) and the content of Fe_1^{3+} and Fe_2^{3+} doublets (**right** panel). Data related to the Fe_1^{3+} and Fe_2^{3+} centers are shown in blue and black colors, respectively. Solid lines are drawn on the eye for ease of perception.

Figure 5 shows the temperature dependencies of the isomer shift for the Fe_1^{3+} and Fe_2^{3+} centers and their common linewidth (in the two-doublet model, it was assumed that the widths of the doublet lines are equal). The positions of the gravity center of the absorption lines for both centers shift toward positive values with decreasing temperature in accordance with the second-order Doppler effect. We also observed a noticeable broadening of the doublet lines at 50 K.
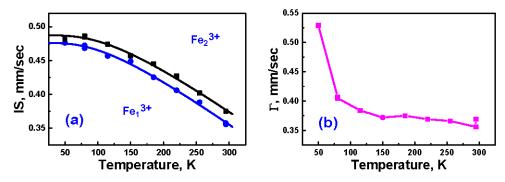

Figure 5. (**a**) Temperature dependencies of the isomer shift (IS) of Fe_1^{3+} and Fe_2^{3+} doublets. Data related to the Fe_1^{3+} and Fe_2^{3+} centers are shown in blue and black colors, respectively. Solid lines are drawn according to Formula (4). (**b**) Temperature dependence of the common line width Γ. Solid magenta line is drawn on the eye for ease of perception.

Figure 6 shows the Mössbauer spectra of $Sr_2FeNbO_{6-\delta}$ in the temperature range from 50 K to 7 K. At 50 K, the spectra still retain the asymmetric doublet structure. These spectra are well fitted using the two-doublet model with a distribution of quadrupole shifts ($\chi^2 \leq 1$). We believe that the observed broadening of the Mössbauer line at 50 K is associated with magnetic correlation for some iron atoms. A solid green line in Figure 6 shows the spectrum corresponding to the ions covered by the magnetic ordering at 50 K. Below 50 K, the Mössbauer spectra fitting was made, taking into account the fact that some of the iron atoms are paramagnetic and some of the atoms are already involved in magnetic ordering. For magnetically ordered ions, the distribution of ultrathin fields was used, and the shape of the lines for the paramagnetic part was a doublet. In order to see how the proportion of these ions varies with temperature, we show a doublet corresponding to paramagnetic ions in the range of 50–7 K on each spectrum.
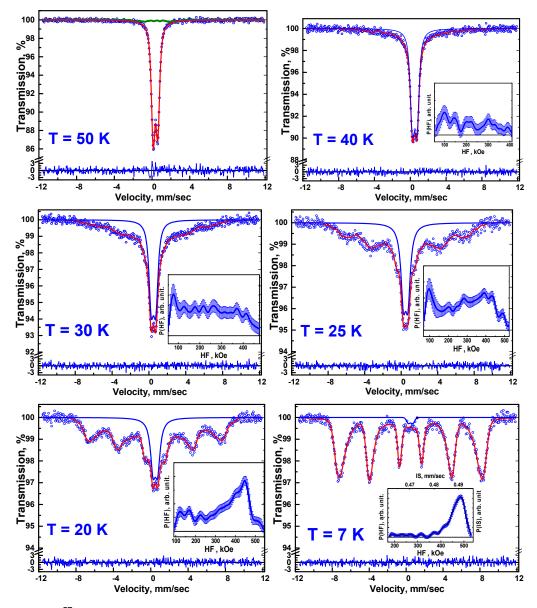
Figure 6. ^{57}Fe Mössbauer spectra of $Sr_2FeNbO_{6-\delta}$ measured at low temperatures: experiments (blue dots) and their best fits (red lines). A solid green line shows the Mössbauer spectrum corresponding to the ions covered by the magnetic ordering at 50 K. The insets show the reconstructed distribution functions of hyperfine parameters IS and HF. Also shown are the differences between the experimental spectra and their best fits normalized to the statistical uncertainty in the range of $\pm 3\sigma$.

However, it should be noted that even for a temperature of 40 K, in order to obtain a fit with a satisfactory value of the χ^2, it was necessary to introduce partial components that contribute to the absorption spectrum in its central part. For low-temperature spectra, such a component is the Zeeman sextet with a distribution of hyperfine parameters.

3.2. Specific Heat

The temperature dependence of the specific heat was measured in the external magnetic fields of 0 and 9 T. The experimental data are shown in Figure 7a. The temperature dependence of the specific heat capacity consists of magnetic and lattice contributions. To identify the magnetic contribution to the specific heat, it is necessary to subtract the

lattice contribution from the experimental data. For this purpose, we decompose the lattice contribution to the specific heat as [23].

$$C_L = \alpha_D \, C_D + \sum_i \alpha_{Ei} C_{Ei}, \tag{1}$$

where C_D is the Debye-specific heat term, and C_E is the Einstein-specific heat term. The Debye term in specific heat data can be defined as

$$C_D = 9R \left(\frac{T}{\theta_D} \right)^3 \int_0^{\frac{\theta_D}{T}} \frac{x^4 e^x dx}{(e^x - 1)^2}. \tag{2}$$

The Einstein term in specific heat data can be defined as

$$C_E = 3R \left(\frac{\theta_E}{T} \right)^2 \frac{exp\left(\frac{\theta_E}{T} \right)}{\left[exp\left(\frac{\theta_E}{T} \right) - 1 \right]^2} \tag{3}$$
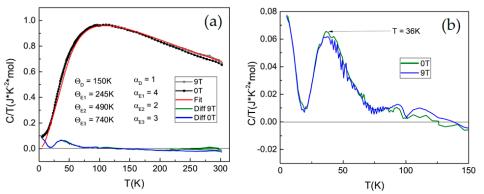

Figure 7. (**a**) Temperature dependencies of the specific heat of $Sr_2FeNbO_{6-\delta}$ experiment (dots), the lattice contribution (red line), and (**b**) the magnetic contribution (blue and green lines) at 0 T (gray dots and green lines) and 9 T (black dots and blue lines).

The lattice contribution C_L can be approximated with a minimum set of fit parameters (four in our case): an isotropic Debye term (C_D) that considers three acoustic phonon branches and three isotropic Einstein terms, which average $3s - 3 = 27$ optical phonon branches. These parameters, extracted from the best fits of the experimental data, are shown in Table 3. The difference between the experimental data and the calculated lattice contribution is the magnetic contribution to the specific heat (Figure 7b). As can be seen from Figure 7b, there are two maxima in the magnetic contribution, at T = 36 K and around 4 K. The number of atoms per formula unit in Sr_2FeNbO_6 is s = 10, so the classical Dulong–Petit saturation value C = 3 Rs, where R = 8.31 J/mol K is the gas constant, is expected to be equal to C = 249.3 J/(mol K).

Table 3. The Debye and Einstein temperatures of $Sr_2FeNbO_{6-\delta}$.

	θ (K)	α
Debye	150	1
Einstein	245	4
	490	2
	740	3

4. Discussion

The asymmetry of the quadrupole lines of Mössbauer spectra can be driven by several reasons, one of which can be related to the texture of the sample at room temperature. To test this assumption, we recorded the spectrum at two orientations of the sample, (i) when the wavevector of the resonant quanta is normal to the sample plane and (ii) when it makes a "magic" angle $\varphi = 54.7°$ with the normal to the sample plane, i.e., at an orientation that equalizes the amplitudes of the doublet lines, if the asymmetry of the lines is due to the texture of the sample. As can be seen from Figure 8, a change in the orientation did not lead to a change in the amplitudes of doublet lines. Therefore, the observed asymmetry can be associated with the presence of centers of iron atoms with different local environments. This assumption is also consistent with the fact that the width of the more intense left doublet line ($\Gamma_L = 0.47$ mm/s) is greater than the width of the right line ($\Gamma_R = 0.43$ mm/s).
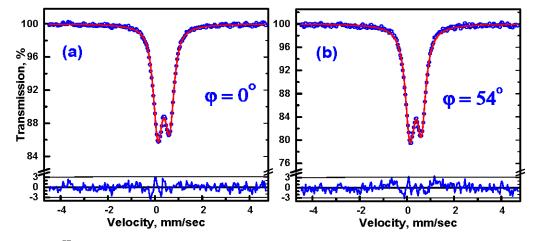

Figure 8. ^{57}Fe Mössbauer spectra of $Sr_2FeNbO_{6-\delta}$ sample measured at room temperature when the wavevector of radiation is normal to the sample plane (**a**) and when it makes a "magic" angle with the normal to the sample plane (**b**): experiments (blue circles) and their best fits (red lines) at room temperature. Also shown are the differences between the experimental spectra and their best fits normalized to the statistical uncertainty in the range of $\pm 3\sigma$.

To determine the number of iron centers and calculate their relative content, the Mössbauer spectrum was fitted under the assumption that there are two doublets with a distribution of quadrupole shifts. The inset in Figure 2a shows the distribution function reconstructed from the experimental spectrum using the SpectrRelax 2.1 software. As can be seen, the distribution function consists of two peaks corresponding to two centers of iron ions in the sample. The isomer shifts of these centers are quite close and correspond to Fe^{3+} ions in an octahedral environment. The distribution peaks for the Fe_1^{3+} at IS ~ 0.356 mm/s, while for the Fe_2^{3+} center, it peaks at IS ~ 0.374 mm/s. Although the isomer shifts of these centers are almost equal, the quadrupole shifts are noticeably different (ε ~ 0.2 mm/s for Fe_2^{3+} and ε ~ 0.3 mm/s for Fe_1^{3+}) and have a wide distribution.

Oxygen octahedral around iron is somewhat deformed from the ideal, according to the space group Pbnm. This leads to the appearance of groups of iron atoms with different local environments. This difference is small, however, in the Mössbauer spectra; it leads to an asymmetry of the experimental doublet spectrum and to the appearance of two Fe^{3+} centers. Of course, the peaks of these centers in the distribution function are blurred due to the influence of Nb^{5+} and non-stoichiometry of the studied sample with oxygen.

Figure 2b,c show the distribution functions of quadrupole shifts for the Fe_1^{3+} and Fe_2^{3+} centers obtained via fitting the experimental spectra using the two-doublet (i.e., two-center) model.

The fitting procedure yielded the values of the isomer shift and the average value of the quadrupole shift at room temperature for Fe_1^{3+} IS = 0.35(6) mm/s and $<\varepsilon>$ = 0.19(8) mm/s, respectively. The hyperfine parameters for the Fe_2^{3+} center are IS = 0.37(4) mm/s and $<\varepsilon>$ = 0.32(0) mm/s, respectively. The Fe_1^{3+} and Fe_2^{3+} centers account for 61% and 39% of the total area of the spectrum, respectively.

The change in the position of the center of gravity of the absorption lines with temperature is determined in the Debye approximation using the function.

$$IS(T) = IS_s(T) - \frac{3kT}{2mc}\left[\frac{3\theta_D}{8T} + 3\left(\frac{T}{\theta_D}\right)^3 \int_0^{\frac{\theta_D}{T}} \frac{x^3}{e^x - 1}dx\right],\tag{4}$$

where the first term $IS_s(T)$ depends on the density of s-electrons in the ^{57}Fe ion, the second term is due to the second-order Doppler effect, m is the mass of the ^{57}Fe nuclide, k is the Boltzmann constant, and c is the speed of light in a vacuum. The first term, which is determined only with the composition and almost independent on temperature, can be considered constant and denoted as IS_s (0). Therefore, the temperature dependence of the absorption-line position, i.e., the isomer shift, is completely determined with the second-order Doppler shift. In Figure 5a, the solid line represents the result of fitting the experimental data using Formula (4). For the identified Fe^{3+} centers, the best fit is achieved with θ_D = 445 ± 6 K and IS_s(0) = 0.59 ± 0.01 mm/s. The θ_D = 445 ± 6 K value is close to the Einstein temperature ~490 K obtained via fitting the temperature dependence of the specific heat capacity.

As can be seen from Figure 6, a decrease in the sample temperature leads to the fact that for some paramagnetic ions the magnetic correlation energy becomes greater than thermal energy. Also, regions of magnetic ordering appear, leading to a decrease in both the intensity and area of doublets and forming a sextet structure of absorption lines for magnetically ordered ions. Figure 9a shows the temperature dependence of the percentage of paramagnetic and magnetically ordered ions in the sample at various temperatures. As can be seen, this process occurs in a temperature range below 40 K due to the existence of magnetic clusters with varied sizes of magnetic correlations.
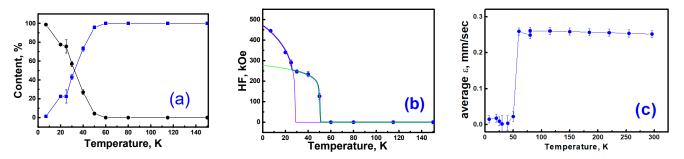

Figure 9. (**a**) Temperature dependencies of the paramagnetic (blue squares) and magnetic contents (black circles), and solid lines are drawn on the eye for ease of perception. (**b**) Temperature dependencies of the average hyperfine magnetic field. Solid violet and green lines are drawn according to Formula (5). (**c**) Temperature dependencies of the average quadrupole shift on ^{57}Fe nuclei.

At 40 K, this component is shown by the blue line (Figure 6). As the temperature decreases, the area of this partial component increases, and already at 25 K and below, it acquires a clear sextet structure whose lines narrow with decreasing temperature (Figure 6). The insets in Figure 6 show the distributions of hyperfine fields, which provide the best fits of the experimental spectra. Along with this magnetic component, even at a temperature of 7 K (Figure 6), the spectra of the $Sr_2FeNbO_{6-\delta}$ sample retain the doublet structure due to paramagnetic Fe^{3+} ions, which are observed at higher temperatures.

Due to this feature, the Mössbauer spectra in the temperature range under consideration demonstrate a complex profile, which is the sum of the contributions from already magnetically ordered ions with a sextet structure and the contributions from ions characterized by a relaxation line shape. In such cases, the method of restoring the distribution of hyperfine parameters is often used to determine the averaged hyperfine parameters from the experimental spectra. The insets in Figure 6 show the distribution functions of hyperfine fields on ^{57}Fe nuclei, which provide the best values of χ^2 for spectra taken at 7, 20, 25, 30, and 40 K.

The uncertainty of the distribution function values is denoted by error bars in Figure 6. As can be seen, the hyperfine magnetic field distribution function is determined with the highest accuracy at 7 K. It features a Gaussian-like shape with asymmetric wings towards low and high magnetic-field values. Figure 9b shows the temperature dependence of the average hyperfine magnetic field on ^{57}Fe nuclei. Unfortunately, the insufficient number of experimental points in the temperature dependence of the average hyperfine magnetic field does not allow us to unambiguously determine the details of the mechanism of antiferromagnetic ordering of iron atoms in this sample. Nevertheless, it follows from Mössbauer measurements at T = 7 K that the sample contains two types of magnetic particles that differ in length and strength of magnetic correlations.

In addition, the magnetic moment of magnetically ordered atoms will depend on the number of nearest Fe neighbors involved in the indirect exchange interaction. As this number decreases, the hyperfine magnetic field on the nucleus decreases, leading to the appearance of contributions to the resonant absorption in the inner part of the spectrum. This feature is characterized in the distribution function of hyperfine fields by the extension of the wing of the Gaussian-like distribution toward weaker magnetic fields. The shape of the temperature dependence of the observed average hyperfine field on Fe^{3+} nuclei suggests the presence of two types of magnetic clusters with different critical ordering temperatures. Figure 9b shows the result of the approximation of the experimental data using the following power function:

$$H_{HF} = H_{1,2} \left(1 - \frac{T}{T_{1,2}} \right)^{b_{1,2}}, \tag{5}$$

where H_1 and H_2 are the values of hyperfine fields at saturation, T_1 and T_2 are the critical temperatures for a given type of magnetic clusters, and b_1 and b_2 are the exponents. The best fits of the experimental data yielded the following values: H_1 = 472 kOe, H_2 = 277 kOe, T_1 = 29 K, T_2 = 50 K, b_1 = 0.25, and b_2 = 0.12. In Figure 9b, these components are shown as solid violet and green lines.

Another feature in low-temperature Mössbauer spectra is the symmetrical shape of the experimental spectra without a clear manifestation of quadrupole splitting. At higher temperatures (T > 50 K), the observed average quadrupole shift is ~0.25 mm/s (Figure 9c). However, with the onset of the magnetic ordering process, i.e., at temperatures below 40 K, the average value of the quadrupole splitting of magnetically ordered ions becomes negligibly small (Figure 9c). As is known, in the presence of a hyperfine magnetic field, the changes caused by the quadrupole splitting strongly depend on both the magnitude and the mutual orientation of the axis of the electric field gradient tensor (EFG) on the nucleus with respect to the direction of the hyperfine magnetic field. When the quadrupole interaction is much weaker than the magnetic hyperfine interaction, the quadrupole splitting can be expressed using the following formula:

$$QS = 2\varepsilon = \frac{1}{8}e^2qQ \left[3\cos^2\theta - 1 + \eta \sin^2\theta \cos 2\varphi \right] \tag{6}$$

where θ and φ are the angles between the direction of the magnetic hyperfine field and the main axis of the EFG tensor. In the case of the random orientation of these vectors, the line shifts caused by the QS quadrupole interaction will be zero on average. Consequently, in

our sample, upon the onset of magnetic ordering, the directions of the magnetic moments of the iron ions, and hence the directions of hyperfine magnetic fields on the Fe nuclei, are randomly distributed with respect to the directions determined with the principal axes of the EFG tensor. Mössbauer spectroscopy showed three different environments around iron [24] for $Sr_2FeMo_{1-x}Nb_xO_6$ compounds at room temperature.

The blurring of the phase transition temperature is confirmed by the specific heat measured in the whole temperature range, which shows no λ-type anomaly that can indicate a transition to a magnetically ordered state.

Figure 7a shows the Cp(T)/T dependence at $B = 0$ and 9 T in temperature range of 4–300 K, where the red line corresponds to the lattice contribution to the specific heat C_{ph}. The blue and green lines show the difference between the experimental values of the specific heat capacity and the lattice contribution. This difference corresponds to the magnetic contribution at magnetic fields 0 and 9 T. For clarity, the magnetic contribution to the specific heat Cm is shown in Figure 7b. The magnetic contribution to the heat capacity demonstrates two maxima, at 4 K and 36 K. The positions of the maxima of the magnetic contribution do not change in the external magnetic field of 9 T. The observation of a peak at 36 K in the magnetic specific heat capacity is consistent with the temperature dependence of average hyperfine magnetic field for one of the magnetic subsystems. This temperature almost coincides with the phase transition temperature T_G = 32.5 K obtained from the discrepancy of the temperature dependence of the magnetic susceptibility measured in ZFC and FC regimes in [13]. The authors of [13] found that below 700 K an extrapolated Curie temperature is negative and is equal to 28 K. The negative value of the Curie temperature indicates the antiferromagnetic nature of the exchange interactions between the spins.

5. Conclusions

Polycrystalline powders of $Sr_2FeNbO_{6-\delta}$ perovskite were synthesized via the solution combustion precursor method. Temperature dependencies of specific heat were measured for the $Sr_2FeNbO_{6-\delta}$ ceramic in the temperature range of 4–300 K at 0 and 9 T. The Mössbauer spectra of $Sr_2FeNbO_{6-\delta}$ were measured in the temperature range from 7 K to room temperature. Low-temperature Mössbauer measurement (at T = 7 K) reveals that the sample contains two types of magnetic structures that differ in the length and strength of magnetic antiferromagnetic correlations. The observed asymmetry of the Mössbauer spectra at room temperature can be associated with the presence in the sample of centers of iron atoms Fe_1^{3+} and Fe_2^{3+} with different local environments. The isomer shift and the average value of the quadrupole shift at room temperature for Fe_1^{3+} are IS = 0.35(6) mm/s and $<\varepsilon>$ = 0.19(8) mm/s, respectively. The Fe_1^{3+} contributes to 61% of the total spectrum area. It was found that the hyperfine parameters for the Fe_2^{3+} center are IS = 0.37(4) mm/s and $<\varepsilon>$ = 0.32(0) mm/s. The two-peak structure of the magnetic contribution to the specific heat and an asymmetric doublet in the Mössbauer spectra indicate the phase separation of the spin system into two subsystems.

Institutional Review Board Statement: Not applicable.

Informed Consent Statement: Not applicable.

Data Availability Statement: All the data obtained in the studies are available on demand.

Conflicts of Interest: The authors declare no conflict of interest. The funders had no role in the design of the study; in the collection, analyses, or interpretation of data; in the writing of the manuscript; or in the decision to publish the results.

References

1. Li, L.; Yan, M. Recent progress in the development of RE2TMTM′O6 double perovskite oxides for cryogenic magnetic refrigeration. *J. Mater. Sci. Technol.* **2023**, *136*, 1–12. [CrossRef]
2. Tailor, N.K.; Listorti, A.; Colella, S.; Satapathi, S. Lead-Free Halide Double Perovskites: Fundamentals, Challenges, and Photovoltaics Applications. *Adv. Mater. Technol.* **2023**, *8*, 2200442. [CrossRef]
3. Liu, X.; Tu, J.; Li, H.; Tian, J.; Zhang, L. Research progress of double perovskite ferroelectric thin films. *Appl. Phys. Rev.* **2023**, *10*, 021315. [CrossRef]
4. Li, X.; Shi, J.; Chen, J.; Tan, Z.; Lei, H. Lead-Free Halide Double Perovskite for High-Performance Photodetectors: Progress and Perspective. *Materials* **2023**, *16*, 4490. [CrossRef]
5. Idris, A.M.; Zheng, S.; Wu, L.; Zhou, S.; Lin, H.; Chen, Z.; Xu, L.; Wang, J.; Li, Z. A heterostructure of halide and oxide double perovskites $Cs_2AgBiBr_6/Sr_2FeNbO_6$ for boosting the charge separation toward high efficient photocatalytic CO_2 reduction under visible-light irradiation. *Chem. Eng. J.* **2022**, *446*, 137197. [CrossRef]
6. Ge, B.; Ma, J.T.; Ai, D.; Deng, C.; Lin, X.; Xu, J. Sr_2FeNbO^6 applied in solid oxide electrolysis cell as the hydrogen electrode: Kinetic studies by comparison with Ni-YSZ. *Electrochim. Acta* **2015**, *151*, 437–446. [CrossRef]
7. Jeong, E.D.; Yu, S.M.; Yoon, J.Y.; Bae, J.S.; Cho, C.R.; Lim, K.T.; Domd, R.; Borsed, H.P.; Kim, H.G. Efficient visible light photocatalysis in cubic Sr_2FeNbO_6. *J. Ceram. Process. Res.* **2012**, *13*, 305–309.
8. Rosas-Huerta, J.L.; Antonio, J.E.; Arévalo-López, E.P.; Muñoz, H.; Marquina, M.L.; Escamilla, R.; Romero, M. Theoretical study of $Sr_2Fe_{1-x}Nb_{1+x}O_6$ system: Electronic and magnetic properties and crystal structure. *J. Phys. Chem. Solids* **2022**, *162*, 110499. [CrossRef]
9. Winterhalder, F.E.; Farzin, Y.A.; Guillon, O.; Weber, A.; Menzler, N.H. Perovskite-Based Materials As Alternative Fuel Electrodes for Solid Oxide Electrolysis Cells (SOECs). *ECS Trans.* **2023**, *111*, 1115. [CrossRef]
10. Maiti, T.; Saxena, M.; Roy, P. Double perovskite $(Sr_2B′B″O_6)$ oxides for high-temperature thermoelectric power generation—A review. *J. Mater. Res.* **2019**, *34*, 107–125. [CrossRef]
11. Yadav, E.; Navale, K.S.; Prajapati, G.L.; Mavani, K.R. Process-Gas-Influenced Anti-Site Disorder and Its Effects on Magnetic and Electronic Properties of Half-Metallic Sr_2FeMoO_6 Thin Films. *Magnetochemistry* **2023**, *9*, 167. [CrossRef]
12. Ciotonea, C.; Hammi, N.; Dhainaut, J.; Marinova, M.; Ungureanu, A.; El Kadib, A.; Michon, C.; Royer, S. Phyllosilicate-derived Nickel-cobalt Bimetallic Nanoparticles for the Catalytic Hydrogenation of Imines, Oximes and N-heteroarenes. *ChemCatChem* **2020**, *12*, 4652–4663. [CrossRef]
13. Shen, Y.; Zhu, Y.; Sunarso, J.; Guan, D.; Liu, B.; Liu, H.; Zhou, W.; Shao, Z. New Phosphorus-Doped Perovskite Oxide as an Oxygen Reduction Reaction Electrocatalyst in an Alkaline Solution. *Chem. A Eur. J.* **2018**, *24*, 6950–6957. [CrossRef]
14. Tezuka, K.; Henmi, K.; Hinatsu, Y.; Masaki, N.M. Magnetic susceptibilities and Mössbauer spectra of perovskites A_2FeNbO_6 (A = Sr, Ba). *J. Solid State Chem.* **2000**, *154*, 591–597. [CrossRef]
15. Rodriguez, R.; Fernandez, A.; Isalgue, A.; Rodriguez, J.; Labrata, A.; Tejada, J.; Obradors, X. Spin glass behaviour in an antiferromagnetic non-frustrated lattice: Sr_2FeNbO_6 perovskite. *J. Phys. C Solid State Phys.* **1985**, *18*, L401. [CrossRef]
16. Kashima, N.; Inoue, K.; Wada, T.; Yamaguchi, Y. Low temperature neutron diffraction studies of Sr_2FeMO_6 (M = Nb, Sb). *Appl. Phys. A* **2002**, *74*, s805–s807. [CrossRef]
17. Rama, N.; Philipp, J.B.; Opel, M.; Chandrasekaran, K.; Sankaranarayanan, V.; Gross, R.; Rao, M.R. Study of magnetic properties of $A_2B′NbO_6$ (A = Ba, Sr, BaSr; and B′ = Fe and Mn) double perovskites. *J. Appl. Phys.* **2004**, *95*, 7528–7530. [CrossRef]
18. Tao; Canales-Vázquez, J.; Irvine, J.T. Structural and electrical properties of the perovskite oxide Sr_2FeNbO_6. *Chem. Mater.* **2004**, *16*, 2309–2316. [CrossRef]
19. Kupriyanov, M.F.; Fesenko, E.G. An X-ray study of the phase transition in Sr_2FeNbO_6. *Kristallografiya* **1961**, *6*, 794.
20. Takeda, T.; Yamaguchi, Y.; Watanabe, H. Magnetic structure of $SrFeO_3$. *J. Phys. Soc. Jpn.* **1972**, *33*, 967–969. [CrossRef]
21. Okuma, H.; Katayama, Y.; Ueno, K. Large Rashba parameter for 4d strongly correlated perovskite oxide $SrNbO_3$ ultrathin film. *arXiv* **2022**, arXiv:2209.09730.
22. Matsnev, M.E.; Rusakov, V.S. SpectrRelax: An application for Mössbauer spectra modeling and fitting. *AIP Conf. Proc.* **2012**, *1489*, 178–185. [CrossRef]
23. Kurbakov, A.I.; Susloparova, A.E.; Pomjakushin, V.Y.; Skourski, Y.; Vavilova, E.L.; Vasilchikova, T.M.; Raganyan, G.V.; Vasiliev, A.N. Commensurate helicoidal order in the triangular layered magnet Na_2MnTeO_6. *Phys. Rev. B* **2022**, *105*, 064416. [CrossRef]
24. Rosas-Huerta, J.L.; Romero, M.; Arévalo-López, E.P.; Antonio, J.E.; Huerta, L.; Pérez-Mazariego, J.L.; Marquina, M.L.; Escamilla, R. Crystal structure, Mössbauer and X-ray photoelectron spectroscopies, and magnetic properties of $Sr_2FeMo_{1-x}Nb_xO_6$ compounds. *J. Solid State Chem.* **2022**, *316*, 123621. [CrossRef]